Rock Mechanics and Rock Engineering (2020) 53:3149–3159
https://doi.org/10.1007/s00603-020-02095-2

ORIGINAL PAPER

An Experimental Study on Scale-Dependent Velocity and Anisotropy in Fractured Media Based on Artificial Rocks with Controlled Fracture Geometries

Pinbo Ding[1,3] · **Ding Wang**[2] · **Xiang-Yang Li**[1,3]

Received: 14 April 2019 / Accepted: 24 March 2020 / Published online: 13 April 2020

Abstract

The scale of the fractures can vary, making the seismic velocity and anisotropy substantially scale dependent. Two mechanisms of the scale-dependent phenomenon may be considered: scattering and wave-induced fluid flow. In this study, we measure the scale-dependent velocity and anisotropy effects through laboratory experiments on porous and non-porous artificial rocks containing aligned fractures. This allows us to isolate the effects of these two mechanisms for the first time, yielding some insights into the scale-dependent phenomenon. For short-wavelength waves, scattering dominates with less wave-induced fluid flow effects. For intermediate- and long-wavelength waves, the P-wave is strongly scale dependent mainly due to wave-induced fluid flow mechanism, and the slow shear-wave is also strongly scale dependent but due to both scattering and wave-induced fluid flow. However, the fast shear-wave is almost scale independent. Moreover, a multi-scale equivalent medium theory can model the P-wave propagation accurately.

Keywords Dispersion · Fluid flow · Velocity anisotropy · Fracture

List of Symbols

λ_P. λ_s	Wavelength of P- and S-waves
d	Fracture scale length
τ_m	Relaxation time at grain scale
τ_f	Relaxation time at fracture scale
η	Fluid viscosity
k	Permeability
c_v	Volume of the individual cracks
K_c	Inverse of the crack space compressibility
c_1	Number of connections to other elements of the pore space
σ_c	Critical stress
μ	Shear-wave modulus
r	Aspect ratio of the crack
ν	Poisson's ratio of the isotropic rock matrix
ς,a_f	Grain size and fracture size
ϕ_p, ϵ_c, ϵ_f	Porosity, crack density and fracture deity
C_{ijkl}	Stiffness tensor of fractured rock
C^0_{ijkl}	Elastic properties of the unfractured porous rock
C^1_{ijkl}, C^2_{ijkl}, C^3_{ijkl}	Contributions from the pores, micro-scale cracks and meso-scale fractures, respectively
λ^0, μ^0	Lame parameters of porous background matrix

1 Introduction

Fractures in underground rocks strongly influence rock properties (Ding et al. 2019; Fan et al. 2013; Li et al. 2015a), and understanding the fracture system within these rocks is critical to a range of geoscience applications such as hydrocarbon exploration, water resource management, CO_2 capture and storage, and geo-thermal exploitation (Fan et al. 2018). Characterizing the fracture system is a difficult task because of its various scales, from pore size to hectometers (Barbier

---

✉ Xiang-Yang Li
xyl1962@hotmail.com

[1] State Key Laboratory of Petroleum Resource and Prospecting, China University of Petroleum (Beijing), Beijing 102249, China

[2] Center of Rock Mechanics and Geohazards, Shaoxing University, Shaoxing 312000, China

[3] CNPC Key Laboratory of Geophysical Exploration, China University of Petroleum (Beijing), Beijing 102249, China

et al. 2012). In some hydrocarbon reservoirs, the dominant fractures are on both the formation scale (10–100 m) and the sector scale (100–1000 m) (Li et al. 2015b; Stephenson et al. 2007). Hydrocarbon reservoir behaviour influenced by large-scale fractures (e.g. decimeter to hectometer) has been examined in real case studies (Cosentino et al. 2002). Previous studies have shown that the influence of fracture geometrical parameters, in particular the fracture scale, is substantial with respect to rock physical properties (de Dreuzy et al. 2001; Liu et al. 2018; Pan et al. 2017; Tran et al. 2006; Wang et al. 2017).

Along with the preferred orientation of minerals (Nicolas and Christensen 1987), sedimentary layering (Backus 1962), micro-cracks, and pores in a non-hydrostatic stress field (Hall et al. 2008), aligned fractures are the main cause of seismic anisotropy that generate directional variations of seismic velocity. The azimuthal information extracted from seismic velocity can be used to investigate the fracture parameters (Boness and Zoback 2004). Observations of amplitude versus azimuth, azimuthal travel time (Wang 2011), attenuation (Ekanem et al. 2013; Li et al. 2019), and shear wave splitting (Al-Harrasi et al. 2011; Verdon and Kendall 2011) can be used to estimate the fracture properties. Nonetheless, distinguishing the fracture parameters at the various scales is still a problem due to heterogeneity and frequency-dependent anisotropy (Chapman 2009; Jiang et al. 2016; Pyrak-Nolte and Nolte 1992).

Scale-dependent seismic properties in fractured media may arise from two potential mechanisms. One is the scattering of seismic waves which is related to the ratio of the seismic wavelength (λ) to the fracture diameter (d). Scale-dependent velocity due to scattering has been widely studied in isotropic media (Berryman 1992) and in anisotropic media (Hudson 1981). The other mechanism is wave-induced fluid flow which is related to the pressure equalization process during seismic wave propagation described by the equivalent medium theory (EMT) in fractured rocks (Berryman 1980; Carcione et al. 1991; Hudson et al. 1996). Based on numerical finite difference forward modelling, previous study pointed out that the effective medium model is qualitatively valid when $\lambda/d > 3$ for shear-wave propagation (Yousef and Angus 2016). Measurements of shear-wave splitting (SWS) are unstable when $1 < \lambda_s/d < 3$, where the scattering is dominant. When $\lambda_s/d < 1$, there is no scale dependency, and the fractured medium becomes transversely isotropic. Previous research discussed the squirt flow mechanism which considers both wave-induced fluid flow and scattering on rough fracture surfaces (Baird et al. 2013). However, there is a lack of experimental studies to validate theoretical and numerical findings due to the difficulties in carrying out laboratory experiments on rocks with controlled fracture geometry, and particularly in isolating the effects of these mechanisms.

In this paper, we fill this gap through the use of two sets of artificial rocks to measure scale-dependent velocity and anisotropy. One set of non-porous artificial rocks contains penny-shaped fractures, and we analyse the scattering effects while the fluid flow effect is absent. In the other set of porous artificial rock in which fractures and pores are saturated by air, we analyse dispersion caused by wave-induced fluid flow in the long-wavelength region where non-porous artificial rocks show scale independence. These laboratory experiments validate previous numerical findings and reveal new insights into the scale-dependent velocity effects due to the two main mechanisms, which forms the basis for characterizing fracture properties using seismic anisotropy.

2 Methods

2.1 Sample Preparation

Artificial rocks have been used to represent fractured rocks in several previous studies. We built two sets of artificial rock samples containing aligned fractures. First, a set of non-porous artificial rocks which is a powder - epoxy mixture with a density of 1.66 g/cm^3, and P- and S-wave velocities of 2920 m/s and 1450 m/s, respectively. When the sample is constructed layer by layer, the penny-shaped inclusions made of rubber (with low P-wave velocity of 1360 m/s, density of 1.09 g/cm^3, S-wave cannot propagate in rubber) are distributed on each layer. Six samples containing different sizes of fractures are constructed. The fracture diameter is 2.50 mm, 3.00 mm, 3.60 mm, 4.30 mm, 5.00 mm, and 6.20 mm, respectively (Fig. 1a).

Then we used a different construction method, based on advances in material science, to build artificial porous sandstones (Ding et al. 2017) that have similar mineral components, pore structure, and cementation to natural rocks. The materials chosen for building artificial porous sandstone are silica sand and clay minerals. We choose sodium silicate as a binder, which provide silicic cementation similar to natural rocks. The mineral powders are mixed in a ball mill for 24 h to ensure homogeneity and then mixed with sodium silicate. The mixture is then poured layer after layer into a 100 × 100 mm mold to create an artificial rock block. When laying the sand mixture in the mold, polymeric material discs are spread out on the surface of each layer. The mold is compressed under 10 MPa for 10 h, then is moved out and heated for 7 days at 80 ℃. After the block has consolidated under these conditions, it is placed into a muffle oven and sintered in a high-temperature environment at 900 ℃. The polymeric material discs decompose into gas and leak out the block under high temperature (900 ℃), leaving penny-shaped voids within the block, simulating fractures.

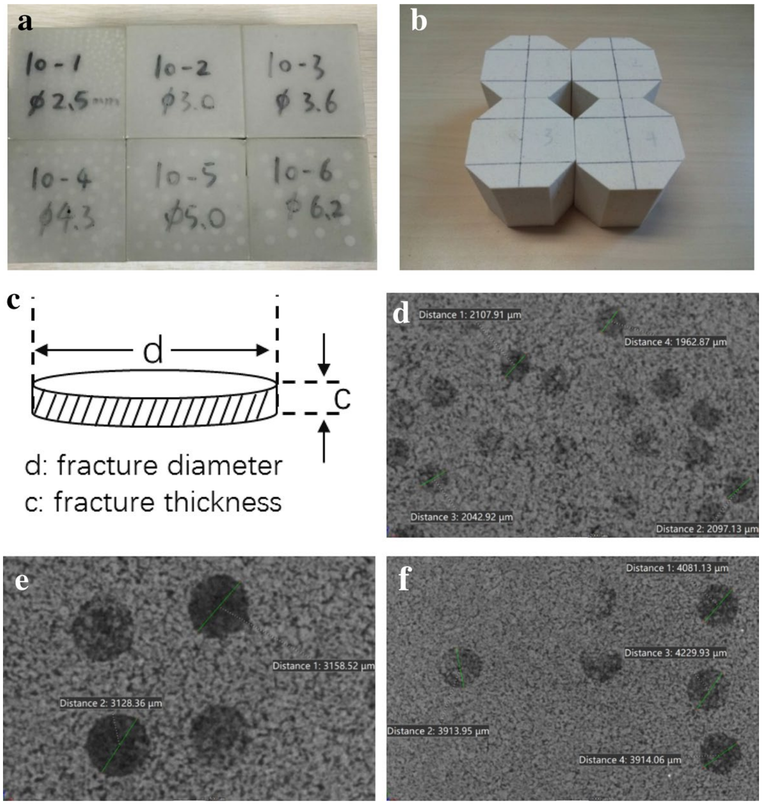

Fig. 1 **a** The non-porous samples with aligned cracks. **b** The porous samples with aligned cracks. **c** The fracture geometries. SEM images of the fracture geometry in the porous samples with 2.00 mm (**d**), 3.00 mm (**e**), 4.00 mm (**f**) fractures

To create artificial rocks with different sizes of fractures, we choose discs with three different diameters and spread them in three different parts of each layer. We set the fracture density at 5%, the fracture thickness at approximately 0.06 mm, and the fracture diameters at 2.00 mm, 3.00 mm, and 4.00 mm, respectively. There is also a sample with no fractures as a reference sample, providing the background properties. After the block was sintered in the oven, it was cut into four blocks with different sizes of fractures. The artificial rock surface is then polished for better coupling with the ultrasonic transducers. Figure 1b shows the completed porous artificial rock samples, and Fig. 1c–f shows the SEM images of the fracture distribution and geometry in the artificial rocks. Figure 2 shows the X-ray CT images of porous artificial rocks. The imbedded fractures are aligned and have same geometries, as described in equivalent medium theories. Compared with the complex fracture parameters in natural rocks, distribution and geometries of the aligned fractures in artificial rocks can be quantitatively controlled. Hence, artificial rocks with aligned fractures can be used to observation the seismic anisotropy affected by fracture parameters, and to validate the equivalent medium theories (Ding et al. 2014, 2017; Tillotson et al. 2014).

2.2 Ultrasonic Measurements

The porous artificial rocks are placed in an oven and dried for 24 h to evaporate any water, leaving air-saturated artificial rocks. According to the test standards of DZ/T0276.24-2015, ultrasonic devices (as shown in Fig. 3) are used to measure the P- and S-wave velocities of the non-porous and porous samples with different fracture sizes. The transmitted P- and S-wave signals are recorded with a digital oscilloscope and a desktop computer. The time sampling interval for all experiments is 0.04 μs for both P- and S-wave signals. Phase velocity is measured in the parallel or perpendicular directions to the symmetry axis (Dellinger and Vernik 1994). Hence, the phase velocities of both P- and S-waves are measured at 0° (e.g. perpendicular to fracture plane) and 90° (e.g. parallel to the fracture plane). The transmitted signals of the reference sample are analysed by Fourier transform to obtain the dominant frequency. The velocities of the matrix are measured from the reference sample, and the wavelength of different frequency is calculated.

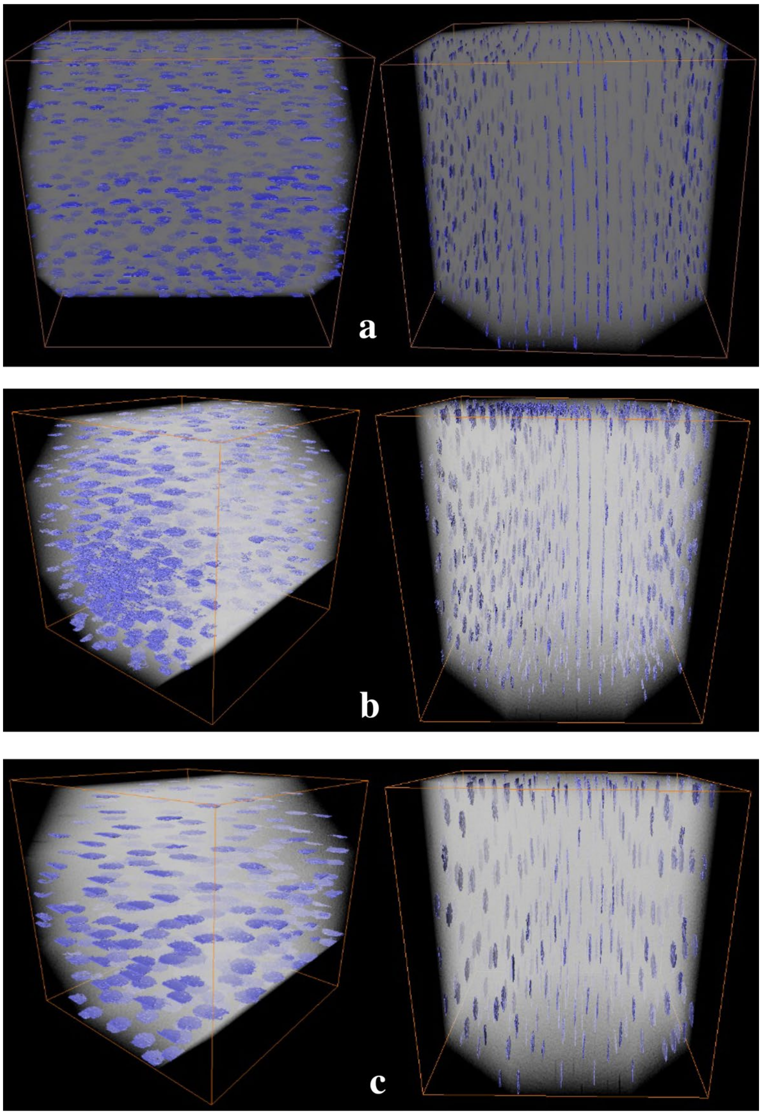

Fig. 2 X-ray CT images of the fracture distribution in the porous samples with 2.00 mm (**a**), 3.00 mm (**b**), and 4.00 mm (**c**) fractures

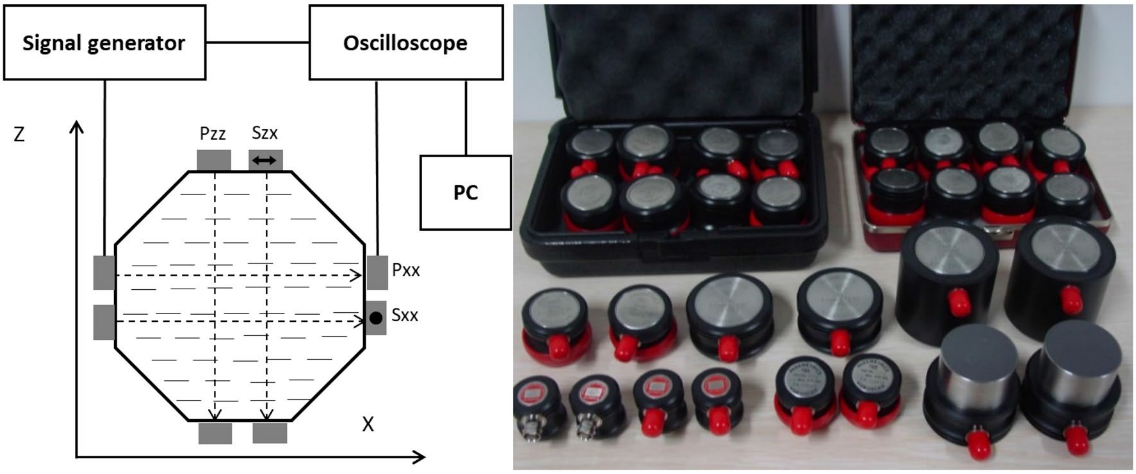

Fig. 3 Schematic diagram for the ultrasonic measurement system and the Olympus ultrasonic transducers

2.3 Modelling the Fluid Flow Effects by the Frequency-Dependent Rock Physics Model

In the frequency-dependent Chapman's model for fractured rocks (Chapman 2003; Chapman et al. 2002), fluid flow takes place at two scales: the grain-scale local flow and the meso-scale inter flow. The grain-scale local flow is related to the squirt flow relaxation time τ_m,

$$\tau_{\mathrm{m}} = \frac{c_{\mathrm{v}}\eta\left(1 + K_{\mathrm{c}}\right)}{\sigma_{\mathrm{c}} k \varsigma c_1}, \tag{1}$$

where η is the fluid viscosity, k is the permeability, c_{v} is the volume of the individual cracks, ς is the grain size, K_{c} is the inverse of the crack space compressibility, c_1 is the number of connections to other elements of the pore space, and $\sigma_{\mathrm{c}} = \pi \mu r/[2(1-v)]$ is the critical stress in which μ is the shear-wave modulus, r is the aspect ratio of the crack, and v is the Poisson's ratio of the isotropic rock matrix. The meso-scale inter flow is related to a larger relaxation time τ_{f} which depends on the fracture size:

$$\tau_{\mathrm{f}} = \frac{a_{\mathrm{f}}}{\varsigma}\tau_{\mathrm{m}} \tag{2}$$

where a_{f} is the fracture size. The overall stiffness tensor is given by

$$C_{\mathrm{ijkl}}(\omega) = C^0_{\mathrm{ijkl}} - \phi_{\mathrm{p}} C^1_{\mathrm{ijkl}} - \epsilon_{\mathrm{c}} C^2_{\mathrm{ijkl}} - \epsilon_{\mathrm{f}} C^3_{\mathrm{ijkl}}, \tag{3}$$

where $\mathrm{C}^0_{\mathrm{ijkl}}$ represents the elastic properties of the unfractured porous rock, and $\mathrm{C}^1_{\mathrm{ijkl}}$, $\mathrm{C}^2_{\mathrm{ijkl}}$ and $\mathrm{C}^3_{\mathrm{ijkl}}$ are the contributions from the pores, micro-scale cracks and meso-scale fractures, respectively. ϕ_{p} is the porosity, ϵ_{c} is the crack density, and ϵ_{f} is the fracture density. The overall elastic properties of the fractured porous rock are functions of the properties of the unfractured porous rock, and crack and fracture densities, as well as the seismic wave frequency and the fluid properties.

Note that the original form of Chapman's model (Chapman 2003; Chapman et al. 2002) is limited to low porosity, following the interaction energy approach of Eshelby' model (Eshelby 1957). Then Chapman's model was modified with no such limitation (Chapman et al. 2003), making the model more applicable to real data. By introducing the λ^0 and μ^0 which were calculated from the measured $\mathrm{V}^0_{\mathrm{p}}$ and $\mathrm{V}^0_{\mathrm{s}}$ and density of the un-fractured rock, a $\mathrm{C}^0_{\mathrm{ijkl}}(\Lambda, \mathrm{M})$ term, a frequency w_0 is added to Eq. (3):

$$C_{\mathrm{ijkl}}(\omega) = C^0_{\mathrm{ijkl}}(\Lambda, \mathrm{M}, w) - \phi_{\mathrm{p}} C^1_{\mathrm{ijkl}}\left(\lambda^0, \mu^0, w\right) - \epsilon_{\mathrm{c}} C^2_{\mathrm{ijkl}}\left(\lambda^0, \mu^0, w\right) - \epsilon_{\mathrm{f}} C^3_{\mathrm{ijkl}}\left(\lambda^0, \mu^0, w\right), \tag{4}$$

where

$$\Lambda = \lambda^0 + \Phi_{\mathrm{c,p}}\left(\lambda^0, \mu^0, w_0\right); \mathrm{M} = \mu^0 + \Phi_{\mathrm{c,p}}\left(\lambda^0, \mu^0, w_0\right), \tag{5}$$

$$\lambda^0 = \rho\left(V^0_{\mathrm{p}}\right)^2 - 2\mu^0; \mu^0 = \rho\left(V^0_{\mathrm{s}}\right)^2. \tag{6}$$

In the case of high porosity, the model is simplified by setting the crack density to zero, Then Eq. (4) becomes

$$C_{\mathrm{ijkl}}(\omega) = C^0_{\mathrm{ijkl}}(\Lambda, \mathrm{M}, w) - \phi_{\mathrm{p}} C^1_{\mathrm{ijkl}}\left(\lambda^0, \mu^0, w\right) - \epsilon_f C^3_{\mathrm{ijkl}}\left(\lambda^0, \mu^0, w\right). \tag{7}$$

Based on the measured parameters of the unfractured rock, fluid properties and fracture parameters, the elastic moduli of the fractured rock can be determined by the above equations. The velocities are then calculated following the Christoffel equations (Cheadle et al. 1991).

The micro-scale relaxation time τ_{m} is a free parameter which should be determined from measured data. The value of τ_{m} is sought that minimized the misfit between the measured data and the theoretical predictions. The minimum value of the relative difference is considered to be the τ_{m} of the micro-scale relaxation time. Figure 4 shows the relaxation time corresponding to the minimum value is $\tau_{\mathrm{m}} = 3.55 \times 10^{-7}$s. Then the estimated τ_{m} is used to generate the theoretical predictions of porous artificial rocks. The input parameters for Chapman' model are the measured data of porous artificial rock with no fractures, the fracture parameters and background properties shown in Table 1, and the estimated relaxation time τ_{m} is as given above.

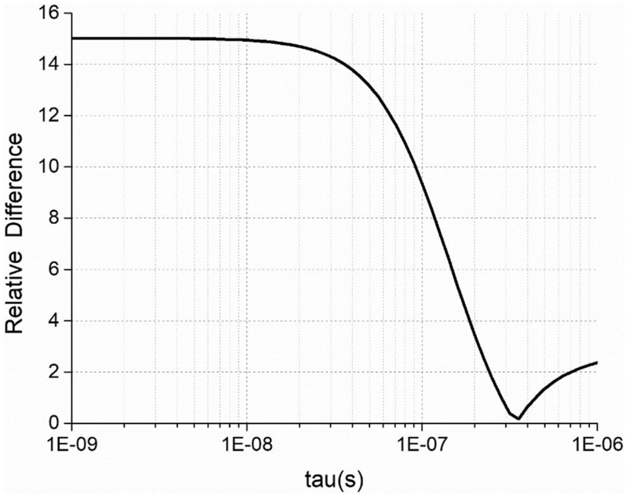

Fig. 4 The estimation of relaxation time τ_m of porous background sample

Table 1 Import parameters of porous samples for Chapman's model

	#1	#2	#3	#4
Fracture density	5.00%	5.00%	5.00%	–
Fracture diameter	2.00 mm	3.00 mm	4.00 mm	–
Fracture thickness	0.06 mm	0.06 mm	0.06 mm	–
Fracture aspect ratio	0.03	0.02	0.015	–
Fluid density	1.29 kg/m^3			
Fluid bulk modulus	0.133 GPa			
Grain size	75 μm			
Fluid viscosity	1 cP			
Permeability	500 mD			

3 Results

3.1 Non-porous Artificial Rocks

The measured results of non-porous artificial rocks show that the P-wave velocity varies significantly with the ratio of the P-wave wavelength to the fracture diameter (λ_P/d), especially in the direction perpendicular to the fractures. When $\lambda_P/d < 14$, as shown in Fig. 5a, P-wave velocity is strongly affected by scattering and decreases with increasing λ_P/d. When $\lambda_P/d > 13$, the P-wave velocity remains unchanged as λ_P/d increases. Figure 5b shows the variations of the S-wave velocity with the ratio of S-wave wavelength to fracture scale (λ_S/d). The fast shear wave velocity shows little variation with λ_S/d overall. However, when $\lambda_S/d < 4$, the slow shear wave velocity decreases sharply with increasing λ_S/d, and when $\lambda_S/d > 3$, the S-wave velocity then becomes stable and shows no variation with λ_S/d.

Figure 5 indicates that the long wavelength limit for P-wave propagation is $\lambda_P/d > 13$ and for S-wave is $\lambda_S/d > 3$. This confirms the numerical findings of previous study (Yousef and Angus 2016). In the intermediate regions ($1 < \lambda_P/d < 14$ and $1 < \lambda_S/d < 4$), Rayleigh scattering affects the P- and S-wave velocity, and phase velocity decreases with increasing λ/d. As the ratio approaches one

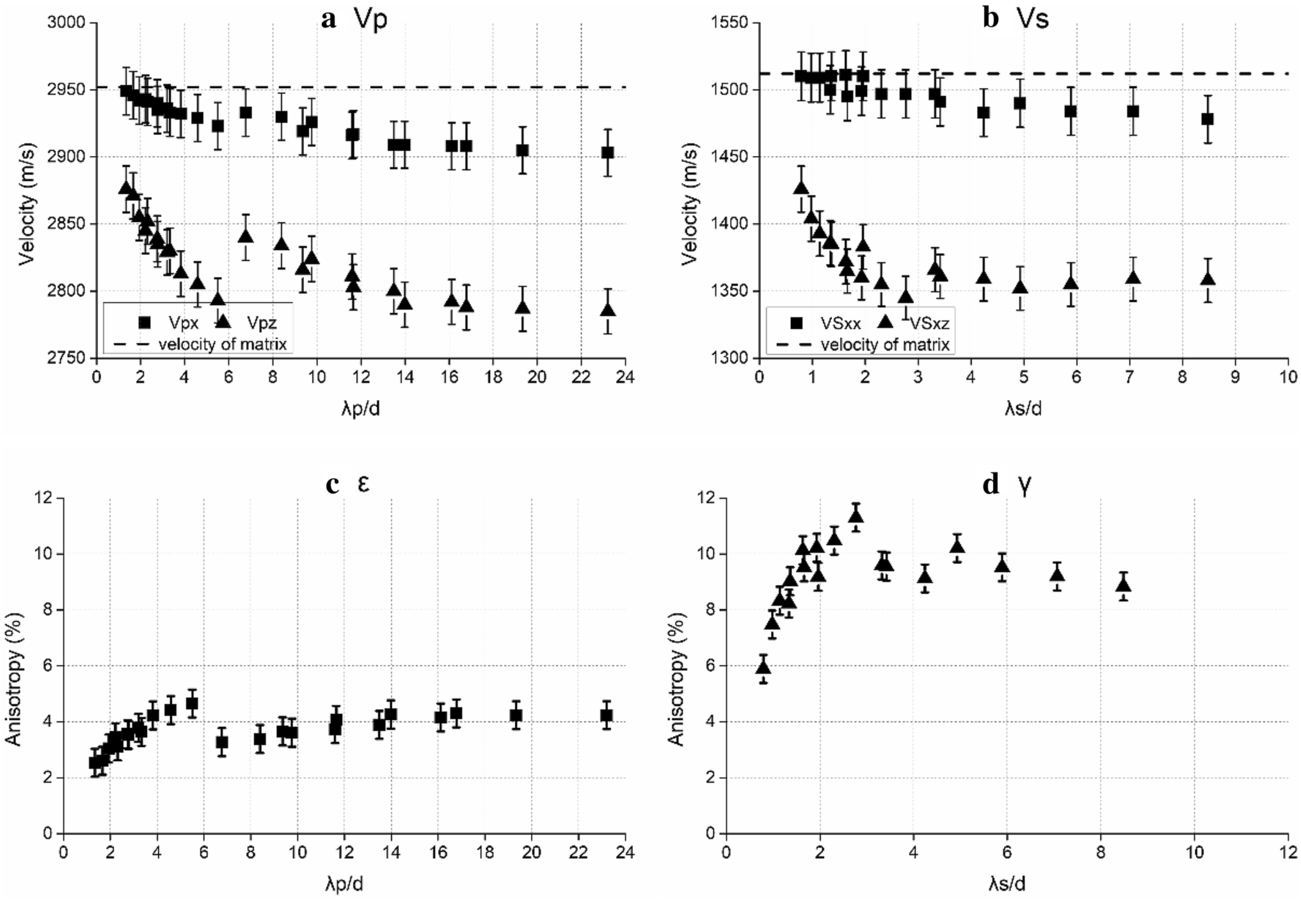

Fig. 5 Experimental results for the non-porous rocks. **a** P-wave velocity. Squares represent velocities in the parallel direction and triangles in the perpendicular direction to the fracture strike. **b** S-wave velocity. Here, squares represent the fast shear wave and triangles represent the slow shear wave. **c**, **d** (Thomsen 1986) parameters ε (squares) and γ (triangles), representing P- and S-wave velocity anisotropies, respectively

$(\lambda/d \approx 1)$, the phase velocity sharply increases due to Mie scattering (Mavko et al. 2009). When $\lambda/d < 1$, the P- and S-wave velocities are scale independent and much higher than in the intermediate- and long-wavelength regions. The ray theory can be used to describe the wave propagation in this case. Note that there is a significant jump in velocity when $\lambda_P/d \approx 2\pi$ in Fig. 5a. A similar phenomenon exists in Fig. 5b when $\lambda_S/d \approx \pi$. This phenomenon is due to the Rayleigh scattering effects. The measured results are in a good agreement with the scale dependence of wave velocity which is related to scattering (Mavko et al. 2009).

As shown in Fig. 5c, d, the P- and S-wave velocity anisotropies are higher in the long-wavelength region than in the short-wavelength region. In the intermediate region, the anisotropy increases with increasing λ/d. The measurement results indicate that the fractured media can be treated as effectively isotropic in the short-wavelength region (Berryman 1992), but it becomes significantly anisotropic in the long-wavelength region. For large faults and joints with the scale length larger than the seismic wavelength, the ray theory is valid to describe the wave propagation. Large amounts of small-scale fractures will introduce significant seismic anisotropy, and equivalent medium theories are valid for describing the wave propagation. In the transition zone, the anisotropy induced by fractures is strongly scale dependent, and if ignored, it may lead to significant uncertainty when inverting fracture parameters from seismic anisotropy.

3.2 Porous Artificial Rocks

Figure 6a, b shows the corresponding measured velocities for the porous artificial rocks. Comparing with Fig. 5, it is apparent that in the short to intermediate region, i.e. $\lambda/d < 14$ for P-wave, and $\lambda/d < 4$ for S-wave, the velocities decrease as λ/d increases, similar to the non-porous case. However, in the long-wavelength region, $\lambda/d > 13$ for the P-wave, and $\lambda/d > 3$ for the S-wave, the velocities continue to decrease as λ/d increases, contrary to the non-porous case. We believe that this is due to the wave-induced fluid flow in the porous artificial rocks.

Note that the non-porous artificial rocks were made of solid epoxy imbedded with rubber discs with no porosity and no fluid flow mechanism, which is suitable for examining the

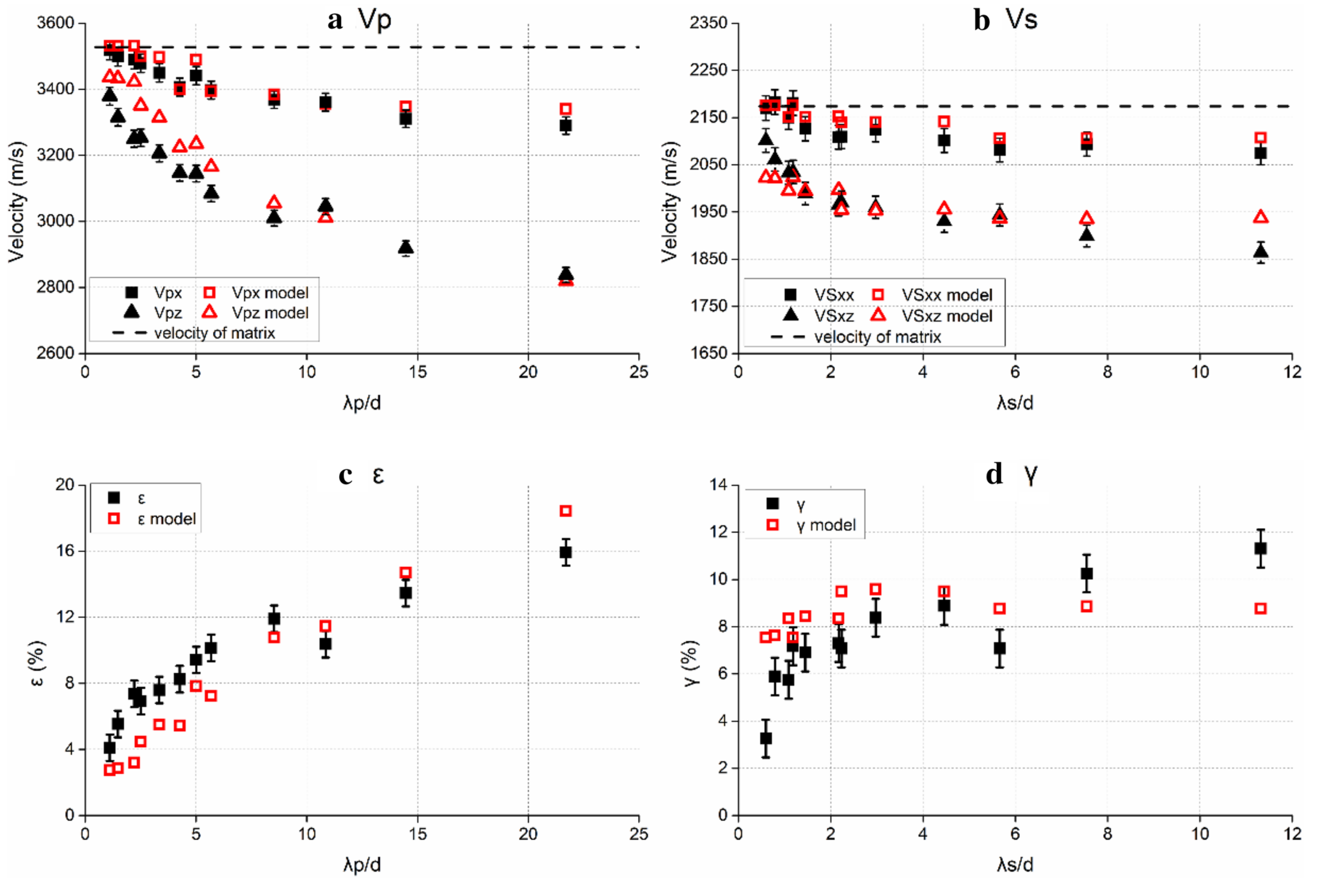

Fig. 6 Experimental results for the porous rocks. The filled symbols represent the measured data, the empty symbols are modelled results. **a** P- and (**b**) S-wave velocities, and (**c**) the Thomsen parameter ε and (**d**) the Thomsen parameter γ

scattering effects. However, in the porous artificial rocks, fractures and pores are saturated by compressible fluid (air in this case). Since the fractures with small aspect ratio are more compressible than pores with large aspect ratio, wave propagation induces a pressure gradient between the pores and fractures, hence generates fluid flow between them. This wave-induced fluid flow makes the wave dispersive and the velocities decrease.

We can also explain this behaviour using the theoretical rock physics model (Chapman 2003; Chapman et al. 2002). First, the fluid interaction occurs at two scales: micro-scale flow in pores and microcracks, and meso-scale flow related to large fractures, which are related to the squirt flow relaxation time τ_m and τ_f, respectively. Hence, the dispersion effects are proportional to the fracture size, and large size fractures yield low characteristic frequency. When the wave frequency is lower than the characteristic frequency, fluid should have sufficient time to flow, making the rock more compressible, with low velocity. Otherwise, when the wave frequency is higher than the characteristic frequency, the unrelaxed fluid makes the rock less compressible, with high velocity. This explains the continuous dispersion of the P-wave velocity for $13 < \lambda_P/d < 21$ and S-wave velocity for $3 < \lambda_S/d < 11$ in Fig. 6a, b. In low-frequency approach, when the wave frequency is considerably lower than the characteristic frequency, rocks present the lowest P-wave velocity due to the fluids in pores and fractures being relaxed.

Second, we can use the Chapman' model to calculate the velocity changes of the porous rocks (shown in Fig. 6). The theoretical results for P-wave velocity at 90° to the fracture normal fit the measured data well, and the P-wave velocity in this direction shows no significant dispersion. At the fracture normal direction, the theoretical results also fit the measured data in the long-wavelength region very well, as shown in Fig. 6a. This confirms the presence of wave-induced fluid flow mechanism in the porous rocks. However, in the intermediate region ($2 < \lambda_P/d < 14$), the theoretical model gives higher predictions of P-wave velocity than the measured values in the fracture normal direction. The disparity between the theoretical results and the measured data indicates the presence of scattering effects in addition to the wave-induced fluid flow effects in this region. In the short-wavelength region, when $\lambda_P/d \approx 1$, or < 1, the equivalent medium theory reaches the high-frequency limit, and the unrelaxed fluids are isolated in pores and fractures. In this case, there is no wave-induced fluid flow effect, and scattering effects are dominant.

The fast shear wave is not significantly affected, as shown in Fig. 6b, implying that the fast shear wave is not sensitive to the fracture scale and wave frequency. Similar to the non-porous artificial rocks, the slow shear wave for the porous artificial rocks presents strong scale-dependent variations. As shown in Fig. 6b, the slow shear wave velocity continues to decrease in the long-wavelength region ($\lambda_S/d > 3$) when the scattering effects are absent, as shown in Fig. 6b. Consequently, the measured shear-wave anisotropy parameter (γ) shows strong scale dependency (Fig. 6d). However, the theoretical red curve at 0° and 90° to the fracture normal shows no change with the fracture scale in the long-wavelength region, and the modelled γ marked with red open triangles is scale independent. This is because in the equivalent medium theory models, the shear modulus is only dependent on the fracture density in the symmetry plane at 0° or 90° to the fracture normal (Chapman 2003; Hudson et al. 2001; Schoenberg and Sayers 1995).

3.3 Scattering Effects

Based on the laboratory results from the non-porous artificial rocks, the scale-dependent velocity and anisotropy caused by scattering effects can be summarized as below:

I. Large-scale faults and joints whose scale length is larger than the seismic wavelength will be highly heterogeneous but possibly isotropic. In this case, the rocks have high velocity and low anisotropy, and the ray theory can be used to describe the wave propagation process.

II. A large amount of small-scale fractures whose scale length is sufficiently long ($\lambda_S/d > 3$ and $\lambda_P/d > 13$) can be treated as homogeneous but anisotropic. In this case, the rocks have low velocity and high anisotropy, and the equivalent medium theory (EMT) can be used to describe the wave propagation process instead.

III. In the intermediate region where Rayleigh scattering ($1 < \lambda_P/d < 14$ and $1 < \lambda_S/d < 4$) and Mie scattering ($\lambda/d \approx 1$) are the dominant effects, seismic velocity and anisotropy are substantially scale dependent. Neither the ray theory nor the EMT is valid to model the wave propagation, and the use of velocity and anisotropy to invert the fracture parameters can contain significant uncertainty.

3.4 Wave-Induced Effects

Based on the laboratory results of the porous artificial rocks, the scale-dependent velocity and anisotropy caused by the wave-induced fluid flow mechanism can be summarized as follows:

I. In the short-wavelength region, when $\lambda/d < 1$, the unrelaxed fluids are isolated in pores and fractures, and there is not sufficient time for the fluid flow. Therefore, there is no wave-induced flow fluid effect similar to the non-porous artificial rocks, and scattering is dominant. Mie scattering ($\lambda/d \approx 1$) is the dominant effect.

II. In the long-wavelength regions ($\lambda_S/d > 3$ and $\lambda_P/d > 13$), the propagating wave induces a pressure gradient between the pores and fractures, causing fluid exchange between them. Therefore, the waves continue to be dispersive. In this case, there are no scattering-related scale-dependent effects, and wave-induced effects are dominant.

III. In the intermediate region ($1 < \lambda_P/d < 14$ and $1 < \lambda_S/d < 4$), the seismic velocity and anisotropy are substantially scale dependent. Their variations are affected by both scattering and wave-induced fluid flow. Consequently, the wave propagation process is more complicated in the intermediate regions compared to the other two regions due to the interactions of these two mechanisms, which are discussed separately in the following section.

Note that the fast shear wave is insensitive to the presence of fluid, and scattering is the only factor to affect the propagation of the fast shear wave. This effect is relatively small and the fast shear wave is almost scale independent.

4 Discussion

To gain some insights into the interaction of these two mechanisms of scale-dependent wave propagation, Fig. 7 shows a comparison of the P-wave velocity in the fracture normal direction in the intermediate region of both the porous and non-porous artificial rocks. The velocity variations of the non-porous artificial rocks are denoted by black solid triangles, illustrating the scattering effects; those of the porous artificial rocks are denoted by black solid squares, illustrating both the scattering and wave-induced effects. The red open squares show the modelled wave-induced fluid flow effects calculated for the porous artificial rocks. The dashed lines through the symbols are calculated by fitting. The slope of the fitted lines represents the degree of the scale dependency and shows the influence of the different mechanisms on the seismic velocity.

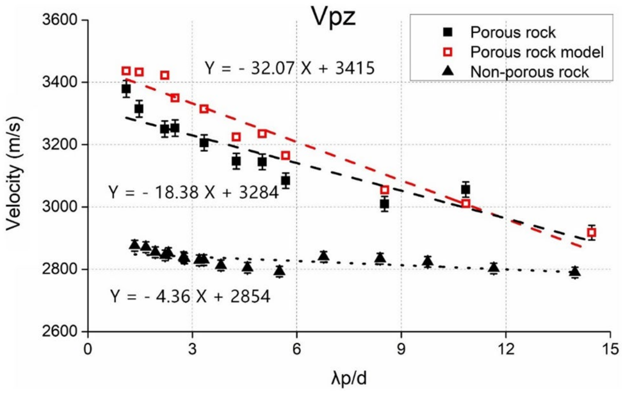

Fig. 7 Comparison of the P-wave velocity in the fracture normal direction in the intermediate region for both porous and non-porous rocks

As shown in Fig. 7, the slope of porous artificial rocks is higher than that of non-porous artificial rock. This indicates that the wave-induced fluid flow introduces more significant velocity variations than scattering. Hence, the fluid flow mechanism is more sensitive to the fracture scale than the scattering mechanism. Also note that the theoretical results (red line) only account for the fluid flow effects and over-predict the amount of dispersion for the porous artificial rocks, indicating that the two mechanisms are competing with each other. Furthermore, the misfit between the measured and modelled data is relatively small, implying that the scattering effects are relatively small and that the Chapman's model (Chapman 2003; Chapman et al. 2002) serves as a good theoretical tool for modelling P-wave propagation in fractured media from the intermediate to the long-wavelength region. This knowledge may have significant implications for characterizing the fracture scale using P-wave anisotropy.

As discussed above, depending on the zones of interest, wave propagation in fractured media is scale dependent and may be influenced simultaneously by both scattering and wave-induced fluid flow. Therefore, considerable care should be taken when using seismic velocity and anisotropy to quantify fractures. Some implications for fracture characterization can be summarized as below:

I. When the seismic wavelength is smaller than fracture scale, conventional seismic imaging and seismic attribute analysis may be directly used to quantify fracture (fault) properties (e.g. fracture strike, density, size, as well as their spatial distribution). The common attributes may include seismic curvature, coherence, dip attribute, etc.

II. In the intermediate region, it is difficult to separate the effects of scattering and wave-induced fluid flow as they may exist simultaneously during wave propagation. However, for P-wave propagation, the scattering effects are relatively small compared with the wave-induced fluid flow effects. In particular, P-wave scale-dependent velocity and anisotropy effects can be modelled relatively accurately using the equivalent medium theories of Chapman's model (Chapman 2003; Chapman et al. 2002) and this makes it possible to quantify the fracture scale based on the P-wave scale-dependent effects. In contrast, shear-wave splitting measurements are more difficult to model in this region, and the accuracy of fracture parameter inversion from γ measurements will be substantially compromised.

III. When wavelength is much larger than fracture size, although imaging individual fractures is not possible, the aggregate properties of the fractured media (e.g. fracture orientation and density) can be inverted from seismic anisotropy. Established procedures include the analysis of azimuthal variations of P-wave attributes, such as AVA (amplitude versus angle), AVOA (amplitude versus offset and azimuth), etc., and the analysis of shear-wave splitting. Observed scale-dependent effects in this region, if any, can be used to quantify the fracture scale, including both scale-dependent P- and S-wave effects.

5 Conclusions

We have observed scale-dependent phenomena influenced by scattering in non-porous artificial rocks, and the laboratory results confirm the previous numerical findings on scale-dependent anisotropy. We compared the scale-dependent velocity and anisotropy of porous artificial rocks (affected by both scattering and fluid flow) and non-porous artificial rocks (no fluid effects), and confirm the presence of wave-induced fluid flow effects in the long-wavelength region when $\lambda_{\mathrm{P}}/d > 13$, where there is no scattering-related scale-dependent effects.

Our experimental results indicate that the fast shear wave is not significantly affected by scattering and fluid flow, but the slow shear wave presents scale dependence in the intermediate-wavelength region. In the intermediate region, scattering and fluid flow both have influences. Their comparison suggests that the fluid flow effects are more significant than the scattering effects, and these two mechanisms compete with each other in terms of the scale-dependent phenomenon. Based on the long-wavelength assumption, Chapman's model gives a good prediction when $\lambda_{\mathrm{P}}/d > 13$. Moreover, Chapman's model still gives a reasonable theoretical prediction in the intermediate wavelength region where the P-wave propagation is affected by both scattering and fluid flow. Our experimental results suggest that Chapman's model can reliably describe the fluid flow effects in most circumstances, and can be used to invert the fracture scale from observed scale-dependent effects.

This study suggests that the scale effects of the fractures to the seismic velocity and anisotropy should be significantly concerned. The scale effects give fundamental insights into fracture characterization in geophysical exploration and rock engineering, such as considering the effects of fracture evolution in hydraulic fracturing can help in improving the accuracy of velocity model in micro-seismic monitoring. However, the fluid flow effects are observed in ultrasonic frequency. The effects of wave-induced fluid flow in kilohertz and seismic frequencies should be observed in laboratory in the future study.

Acknowledgements This work is supported by the National Natural Science Fund Projects (41804105, U19B6003), the Fundamental Research Funds for the Central Universities (2462018YJRC008) and the National Science and Technology Major Project (2017ZX05018005).

Compliance with Ethical Standards

Conflict of interest The authors declare that they have no conflict of interest.

References

Al-Harrasi OH, Kendall J-M, Chapman M (2011) Fracture characterization using frequency-dependent shear wave anisotropy analysis of microseismic data. Geophys J Int 185(2):1059–1070

Backus GE (1962) Long-wave elastic anisotropy produced by horizontal layering. J Geophys Res 67(11):4427–4440

Baird A, Kendall J, Angus D (2013) Frequency-dependent seismic anisotropy due to fractures: fluid flow versus scattering. Geophysics 78(2):WA111–WA122

Barbier M, Hamon Y, Callot J-P, Floquet M, Daniel J-M (2012) Sedimentary and diagenetic controls on the multiscale fracturing pattern of a carbonate reservoir: The Madison Formation (Sheep Mountain, Wyoming, USA). Mar Petrol Geol 29(1):50–67

Berryman JG (1980) Long-wavelength propagation in composite elastic media II. Ellipsoidal inclusions J Acoust Soc Am 68(6):1820–1831

Berryman JG (1992) Single-scattering approximations for coefficients in Biot's equations of poroelasticity. J Acoust Soc Am 91(2):551–571

Boness NL, Zoback MD (2004) Stress-induced seismic velocity anisotropy and physical properties in the SAFOD Pilot Hole in Parkfield. CA Geophys Res Lett 31(15):L15S17

Carcione J, Kosloff D, Behle A (1991) Long-wave anisotropy in stratified media: a numerical test. Geophysics 56(2):245–254

Chapman M (2003) Frequency-dependent anisotropy due to meso-scale fractures in the presence of equant porosity. Geophys Prospect 51(5):369–379

Chapman M (2009) Modeling the effect of multiple sets of mesoscale fractures in porous rock on frequency-dependent anisotropy. Geophysics 74(6):D97–D103

Chapman M, Maultzsch S, Liu E, Li XY (2003) The effect of fluid saturation in an anisotropic multi-scale equant porosity model. J Appl Geophys 54(3):191–202

Chapman M, Zatsepin SV, Crampin S (2002) Derivation of a microstructural poroelastic model. Geophys J Int 151(2):427–451

Cheadle SP, Brown RJ, Lawton DC (1991) Orthorhombic anisotropy: A physical seismic modeling study. Geophysics 56(10):1603–1613

Cosentino L et al (2002) Integrated study of a fractured Middle East reservoir with stratiform super-K intervals-part 2: upscaling and dual-media simulation. Spe Reserv Eval Eng 5(01):24–32

de Dreuzy J-R, Davy P, Bour O (2001) Hydraulic properties of two-dimensional random fracture networks following a power law length distribution: 1. Effective Connectivity Water Resour Res 37(8):2065–2078

Dellinger J, Vernik L (1994) Do travel times in pulse-transmission experiments yield anisotropic group or phase velocities? Geophysics 59(11):1774–1779

Ding P, Di B, Wang D, Wei J, Li X (2014) P and S wave anisotropy in fractured media: experimental research using synthetic samples. J Appl Geophys 109:1–6

Ding P, Di B, Wang D, Wei J, Li X (2017) Measurements of seismic anisotropy in synthetic rocks with controlled crack geometry and different crack densities. Pure Appl Geophys 174(5):1907–1922

Ding P, Wang D, Di G, Li X (2019) Investigation of the effects of fracture orientation and saturation on the Vp/Vs ratio and their implications. Rock Mech Rock Eng 52(9):3293–3304

Ekanem AM, Wei J, Li X-Y, Chapman M, Main IG (2013) P-wave attenuation anisotropy in fractured media: a seismic physical modelling study. Geophys Prospect 61(s1):420–433

Eshelby JD (1957) The determination of the elastic field of an ellipsoidal inclusion, and related problems. Proc R Soc Lond A 241(1226):376–396

Fan LF, Gao JW, Wu ZJ, Yang SQ, Ma GW (2018) An investigation of thermal effects on micro-properties of granite by X-ray CT technique. Appl Therm Eng 140:505–519

Fan LF, Yi XW, Ma GW (2013) Numerical manifold method (NMM) simulation of stress wave propagation through fractured rock mass. Int J Appl Mech 05(02):1350022

Hall SA, Kendall J-M, Maddock J, Fisher Q (2008) Crack density tensor inversion for analysis of changes in rock frame architecture. Geophys J Int 173(2):577–592

Hudson JA (1981) Wave speeds and attenuation of elastic waves in material containing cracks. Geophys J R Astr Soc 64(1):133–150

Hudson JA, Liu E, Crampin S (1996) The mechanical properties of materials with interconnected cracks and pores. Geophys J Int 124(1):105–112

Hudson JA, Pointer T, Liu E (2001) Effective-medium theories for fluid-saturated materials with aligned cracks. Geophys Prospect 49(5):509–522

Jiang H-Y, Chen Z-B, Zeng X-X, Lv H, Liu X (2016) Velocity calibration for microseismic event location using surface data. Pet Sci 13(2):225–236

Li JC, Li HB, Zhao J (2015a) An improved equivalent viscoelastic medium method for wave propagation across layered rock masses. Int J Rock Mech Min Sci 73:62–69

Li JC, Liu TT, Li HB, Liu YQ, Liu B, Xia X (2015b) Shear wave propagation across filled joints with the effect of interfacial shear strength. Rock Mech Rock Eng 48(4):1547–1557

Li JC, Rong LF, Li HB, Hong SN (2019) An SHPB test study on stress wave energy attenuation in jointed rock masses. Rock Mech Rock Eng 52:403–420

Liu RC, Jiang YJ, Huang N, Sugimoto S (2018) Hydraulic properties of 3D crossed rock fractures by considering anisotropic aperture distributions. Adv Geo-Energy Res 2(2):113–121

Mavko G, Mukerji T, Dvorkin J (2009) The rock physics handbook: tools for seismic analysis of porous media, 2nd edn. Cambridge University Press, California

Nicolas A, Christensen NI (1987) Formation of anisotropy in upper mantle peridotites—a review. In: Fuchs K, Froidevaux C (eds) Composition, structure and dynamics of the lithosphere-asthenosphere system. American Geophysical Union, pp 111–123. doi: 10.1029/GD016p0111

Pan B-Z, Yuan M-X, Fang C-H, Liu W-B, Guo Y-H, Zhang L-H (2017) Experiments on acoustic measurement of fractured rocks and application of acoustic logging data to evaluation of fractures. Pet Sci 14(3):520–528

Pyrak-Nolte LJ, Nolte DD (1992) Frequency dependence of fracture stiffness. Geophys Res Lett 19(3):325–328

Schoenberg M, Sayers CM (1995) Seismic anisotropy of fractured rock. Geophysics 60(1):204–211

Stephenson BJ, Koopman A, Hillgartner H, McQuillan H, Bourne S, Noad JJ, Rawnsley K (2007) Structural and stratigraphic controls on fold-related fracturing in the Zagros Mountains, Iran: Implications for reservoir development. In: Lonergan L, Jolly RJH, Rawnsley K, Sanderson DJ (eds) Fractured Reservoirs, vol 270. vol 1. Geological Society, London, pp 1–21. doi: 10.1144/gsl.sp.2007.270.01.01

Thomsen L (1986) Weak elastic anisotropy. Geophysics 51(10):1954–1966

Tillotson P, Chapman M, Sothcott J, Best AI, Li X-Y (2014) Pore fluid viscosity effects on P- and S-wave anisotropy in synthetic silica-cemented sandstone with aligned fractures. Geophys Prospect 62(6):1238–1252

Tran NH, Chen Z, Rahman SS (2006) Integrated conditional global optimisation for discrete fracture network modelling. Comput Geosci-UK 32(1):17–27

Verdon JP, Kendall JM (2011) Detection of multiple fracture sets using observations of shear-wave splitting in microseismic data. Geophys Prospect 59(4):593–608

Wang D, Qu SL, Zhao Q, Yin XY, Zhou F (2017) Laboratory studies of ultrasonic wave response of fractures with different lengths: Anisotropy characteristics and coda analysis. Ultrasonics 80(Supplement C):101–112

Wang Y (2011) Seismic anisotropy estimated from P-wave arrival times in crosshole measurements. Geophys J Int 184(3):1311–1316

Yousef BM, Angus DA (2016) When do fractured media become seismically anisotropic? Some implications on quantifying fracture properties. Earth Planet Sc Lett 444:150–159